

Detection of cloud-affected AIRS channels using an adjacent-pixel approach

By J. JOINER^{1*}, P. POLI^{1,2,3}, D. FRANK^{1,4} and H. C. LIU^{1,5}

¹NASA Goddard Space Flight Center Laboratory for Atmospheres, USA

²University of Maryland, USA

³Centre National de Recherches Météorologiques, Météo France, Toulouse, France

⁴Decisions Systems Technologies Inc., USA

⁵Science Applications International Corporation, USA

(Received 9 June 2003; revised 20 October 2003)

SUMMARY

High-spectral-resolution infrared sounders such as the Atmospheric InfraRed Sounder (AIRS), flying on the National Aeronautics and Space Administration Earth Observing System (EOS) Aqua satellite, provide information about vertical temperature and humidity structure that is potentially useful for data assimilation and numerical weather prediction. Tropospheric channels from infrared sounders are frequently affected by cloud. The methods currently used operationally to account for cloud effects are screening to eliminate cloud-contaminated data and cloud-clearing. For either approach, it is important to determine which channels peak sufficiently above the cloud so that they are not contaminated. Depending on the sounding, different combinations of channels are cloud-contaminated, thus making cloud detection difficult.

This paper proposes a new method of identifying clear or unaffected channels using adjacent pixels. Unlike other proposed or implemented methods, this approach does not rely heavily on having accurate background information about the atmospheric state or estimates of its error. The method also does not make any assumptions about cloud spectral properties. Instead, it assumes that clouds will produce adjacent-pixel variability. The approach requires an estimate of clear-scene adjacent-pixel homogeneity that can be obtained with real data.

We apply the methodology to simulated AIRS data using Monte Carlo experiments. We then apply the algorithm to real AIRS data and use brightness temperature departure statistics as an independent check for residual cloud contamination. We also make qualitative comparisons with cloud properties derived from the EOS Aqua Moderate-Resolution Imaging Spectroradiometer instrument.

KEYWORDS: Assimilation High resolution Radiances

1. INTRODUCTION

The high spectral resolution of advanced infrared sounders, such as the Atmospheric InfraRed Sounding (AIRS) (Aumann and Pagano 1994), should result in significantly improved temperature- and moisture-sounding capabilities as compared with the current operational High-resolution InfraRed Sounder (HIRS) (e.g. Joiner and da Silva 1998; Prunet *et al.* 1998). Therefore, AIRS has the potential to improve numerical weather prediction (NWP) forecasts. Several NWP centres now receiving AIRS data in near real time are starting to monitor the data and conduct impact studies. AIRS is flying with the Advanced Microwave Sounding Unit-A (AMSU-A) and the Humidity Sounder for Brazil on the National Aeronautics and Space Administration (NASA) Earth Observing System (EOS) Aqua platform.

Infrared data are frequently affected by cloud. Therefore, observations must be processed for operational data assimilation, either by screening to remove cloud-contaminated pixels as in e.g. Derber and Wu (1998), or by cloud-clearing to remove the effect of cloud as in e.g. Joiner and Rokke (2000). Although efforts are underway to assimilate cloud information from infrared sounders (e.g. Chevallier *et al.* 2002), operational NWP centres currently use cloud-screened or cloud-cleared data.

Cloud-clearing uses adjacent pixels to estimate clear-column radiances that would have been observed in the absence of cloud (Smith 1968; Chahine 1974, 1977).

* Corresponding author: Laboratory for Atmospheres, NASA Goddard Space Flight Center, Greenbelt, MD, 20771, USA. e-mail: joiner@gsfc.nasa.gov

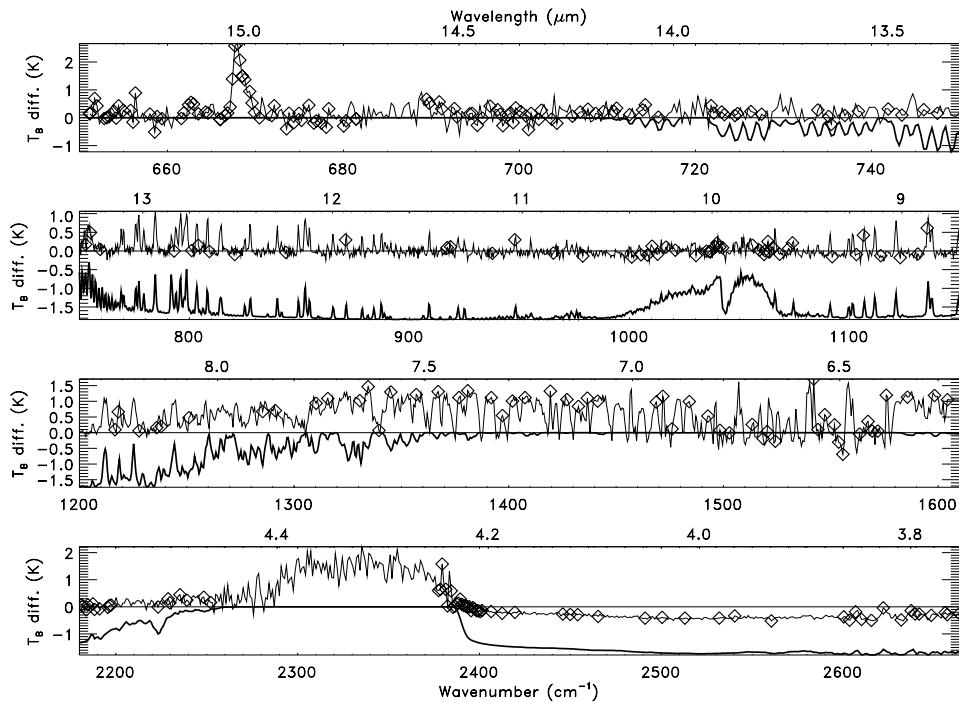


Figure 1. Simulated brightness temperature difference spectra at AIRS resolution. Light line: simulated noisy cloudy observations (black cloud at 800 hPa with 30% cloud fraction) minus background that assumed clear conditions with background errors (background skin-temperature error of -2.3 K); heavy line: true clear minus cloudy; diamond: channel provided in the near-real-time dataset.

This process amplifies random measurement noise and should only be applied to cloud-affected channels. Therefore, it is important both for cloud-clearing and cloud-screening to determine how many channels of a given sounding are cloud-affected.

There are several methods that have been used to detect cloud-contaminated radiance measurements or to determine the height of a cloud and thus which channels peak above the cloud. Specifically, the methods that are being developed for application of AIRS to data assimilation include variational cloud detection (English *et al.* 1999), cloud pressure and effective fraction determination assuming black (unity emissivity) cloud (J. Derber 2002, personal communication), and a digital filtering approach (McNally and Watts 2003). A CO_2 slicing method has been applied to low-spectral-resolution infrared sounders (e.g. Menzel *et al.* 1992). All of these approaches make use of a background or prior estimate of atmospheric temperature, humidity, ozone, and surface skin temperature to estimate the clear radiance. Some of the methods require an estimate of the background error. In addition, some of the algorithms may impose assumptions about cloud spectral properties.

In cases of small to moderate fractions of low cloud, observed brightness temperatures can be significantly reduced as compared with a clear scene. At the same time, it is possible to have relatively small skin-temperature error in the background that can mimic the effect of the cloud. In such a case, a cloudy scene or cloud-affected channels may prove difficult to distinguish from clear if only examined from an observed-minus-background ($O - B$) point of view.

Figure 1 shows simulated brightness temperature differences (single cloud level) for such a case: an 800 hPa black cloud with a 30% fractional amount. The atmospheric situation was a model-generated midlatitude summer profile. Similar results are obtained for a 700 hPa cloud with a 23% fraction. Differences of ~ 0.5 – 1.0 K are comparable to background errors projected into brightness temperature space (as shown in appendix A for channels in the $15\ \mu\text{m}$ band) and thus may be mistaken as such, especially when only a subset of channels is available, although the full spectral patterns may be different. Similar scenarios can occur for lower cloud fractions (e.g. 20%) where a smaller error in skin temperature (~ 1.5 K) mimics the cloud effect.

We have developed an alternative approach that requires a different set of assumptions. The method assumes that clouds will produce variability in adjacent-pixel radiances for affected channels. It does not rely heavily on having accurate background information, and it does not make assumptions about the spectral properties of the cloud. Spatial coherency has been previously exploited for cloud detection, although not on a channel-by-channel basis, using infrared (IR) sounders and imagers (e.g. Masiello *et al.* 2003).

Section 2 describes the algorithm in detail. Results from studies using simulated AIRS data are discussed in section 3. We apply the methodology to real AIRS data in section 4 and use $O - B$ statistics as an independent verification. Finally, we provide qualitative comparisons with collocated data from the NASA EOS-Aqua Moderate-Resolution Imaging Spectroradiometer (MODIS). Conclusions and suggestions for further research are given in section 5.

2. METHODOLOGY

The NASA Global Modeling and Assimilation Office (GMAO) is currently receiving a reduced AIRS radiance dataset in near real time (Goldberg *et al.* 2003) provided by the National Oceanic and Atmospheric Administration National Environmental Satellite Data and Information Service. This dataset contains a 281 channel subset of the 2378 available AIRS channels. There are nine AIRS pixels within an AMSU-A footprint as depicted in Fig. 2. The combined AIRS/AMSU pixels are known as a ‘golfball’. The dataset retains half of the available golfballs. The GMAO receives all nine pixels, whereas other NWP centres currently receive only the centre AIRS pixel within a golfball.

(a) *Determining the significance of adjacent-pixel variability for cloud detection*

We must first decide how to use the nine golfball pixels. The pixels within each golfball column have the same satellite zenith angle (SZA). The SZAs vary slightly between the columns. Changes in SZAs effectively move the channel weighting functions up and down in the atmosphere due to changes in the atmospheric path for a given altitude. Therefore, if the pixels within a golfball are completely cloud free, brightness temperature differences between the columns will occur owing to the different SZAs.

For this study we use only one column per golfball in order to ensure consistent SZAs. We choose the column that contains the pixel with the highest temperature in an $11\ \mu\text{m}$ window channel. This pixel will later be referred to as the ‘first pixel’. The other columns are discarded as shown in Fig. 2.

Our original implementation attempted to use all nine pixels with an eigenvector decomposition to reduce the nine pixels to three fields of view (FOVs) such that the radiance contrast between the FOVs was maximized. We found that, in addition to the positive attribute of enhancing contrast due to clouds, the decomposition also increased

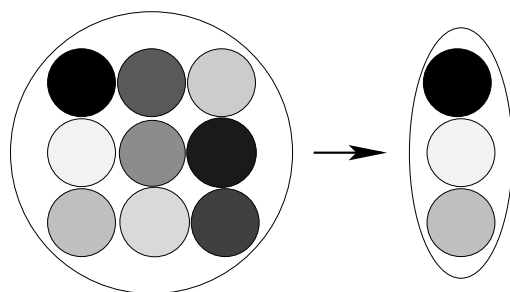


Figure 2. Schematic view of the contrast within the nine AIRS pixels contained in the AMSU footprint ('golfball'), and the pixels chosen for this study. Darker shadings represents higher brightness temperatures in the $11\ \mu\text{m}$ window.

contrast due to SZA differences. This effect was greater at the scan edges where the brightness temperature differences due to SZA variations are at a maximum. Efforts to account for SZA effects greatly complicated the algorithm. The eigen-decomposition also amplifies random instrument noise. Although this effect can be properly taken into account, it is another complication.

The next step is to compute the radiance differences between the first pixel and the two other pixels in the column for channels with a surface-to-space transmittance τ_s between 0.1 and 0.5. The weighting functions of these channels peak near or just above the surface. The contrast is defined as significant when, for all of these channels, the adjacent-pixel brightness temperature differences exceed 0.5 K for either pixel combination. Slightly less than half of the time, significant variability is observed. As we will see in section 4, relatively good overall coverage is obtained. The contrast test is designed to be conservative such that the algorithm will tend to err by declaring scenes with contrast as 'no contrast', rather than vice versa which may allow overcast scenes into the algorithm based on a single noisy observation.

For completeness, we briefly present the tests used to determine whether a pixel is cloud free if there is no significant contrast. These tests are along the lines of Joiner and Rokke (2000) and McMillin and Dean (1982). They verify that a single channel ($11\ \mu\text{m}$) surface skin temperature retrieval agrees with the background to within ± 1 K over ocean and ± 3 K over land. In addition, $11\ \mu\text{m}$ - and $3.8\ \mu\text{m}$ -retrieved skin temperatures must agree to within ± 1 K at night and those from $11\ \mu\text{m}$ and $12\text{--}13\ \mu\text{m}$ to within ± 1 K at all times.

These tests are passed only about 4% of the time. If the contrast test is not applied and the clearest golfball pixel is subjected to the other checks, scenes are declared clear about 10% of the time. If the contrast test is applied to all nine pixels within a golfball in addition to the other tests, the scene is found to be clear less than 2% of the time. If a pixel does not pass the clear tests, the cloud pressure is conservatively set to 100 hPa.

(b) Channel selection for clear-channel identification

We next define a subset of channels to be used in determining whether a cloud is present at a given level. These channels are primarily sensitive to CO_2 absorption and less sensitive to absorption from other constituents such as water vapour and O_3 . The latter constituents have larger uncertainties in their concentrations and may present higher horizontal variability than CO_2 . Therefore, there is greater uncertainty in the weighting functions of channels sensitive to water vapour and O_3 , rather than to those sensitive primarily to CO_2 . The weighting functions for channels in CO_2 absorption

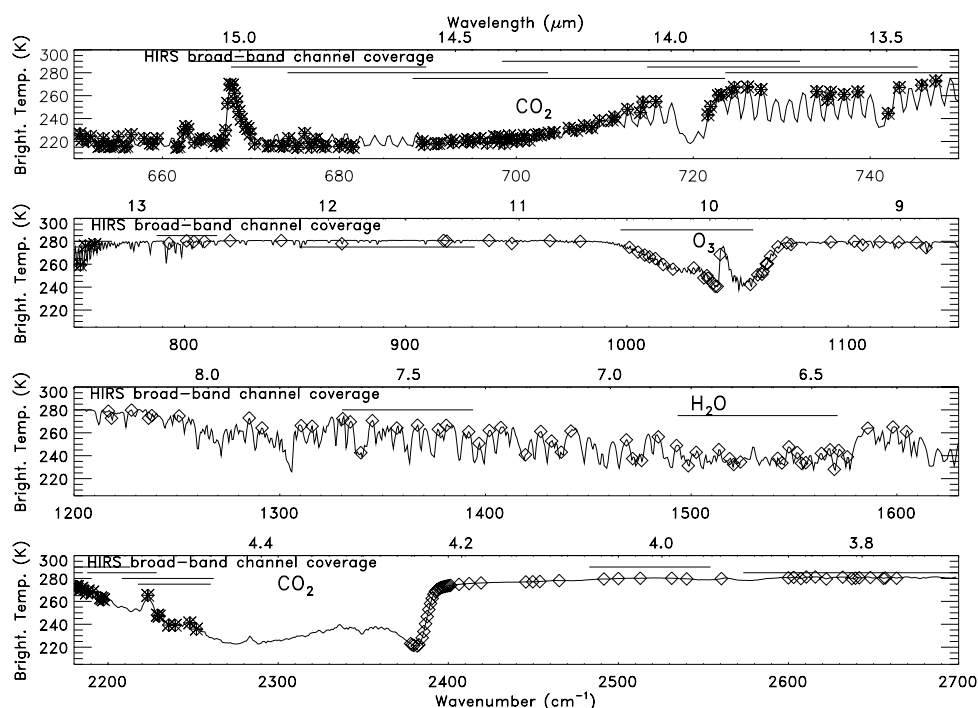


Figure 3. Simulated brightness temperature spectrum at AIRS resolution. Major absorption bands are indicated above along with frequency bands of HIRS channels (solid horizontal lines). Star: channel used in cloud detection algorithm; diamond: channel provided in the near-real-time dataset.

bands (primarily used for temperature sounding) can be computed accurately from a background assuming a fixed CO_2 concentration. The calculation of τ_s and weighting functions is the only instance where background information is used in our cloud detection algorithm when there is significant variability.

The selected channels are those within wave-number bands $650\text{--}790\text{ cm}^{-1}$ and $2180\text{--}2349\text{ cm}^{-1}$. Figure 3 shows a simulated night-time brightness temperature spectrum at AIRS resolution. The available channels in the near-real-time dataset are shown along with the subset used in our cloud detection algorithm. For reference, we indicate the important absorption bands and the frequency bands of HIRS channels.

There are 134 available channels from our set of 281 AIRS channels that fall within these bands (although about 10 of these in the strongest part of the $15\text{ }\mu\text{m}$ band always peak above the clouds and do not get used by the algorithm). The short-wavelength side of the $4.3\text{ }\mu\text{m}$ band could also be used, but it only provides a few channels that are not affected by non-local thermodynamic equilibrium that occurs in daylight.

(c) Clear-channel identification

In clear-scene conditions, the variations in adjacent-pixel radiances include contributions from instrument noise as well as atmospheric and surface variability. The algorithm uses a single test to determine whether adjacent-pixel variability exceeds that expected in clear conditions.

The algorithm starts from the 100 hPa level and steps downwards to lower atmospheric levels until a cloud is found or the surface is reached. There are 100 levels

TABLE 1. PARAMETERS USED IN CLOUD DETECTION ALGORITHM AND EXPERIMENTAL RESULTS INVOLVING TRUE (RETRIEVED) CLOUD PRESSURE P_{true} (P_{ret}). ALL PRESSURES IN hPa AND ΔP REPRESENTS A PRESSURE OFFSET.

z	Max. BT error	No. of cases BT error > 0.1 K	Max. P_{ret}	$p(P_{\text{ret}} > P_{\text{true}} + \Delta P)$		$p(P_{\text{ret}} < P_{\text{true}} - \Delta P)$	
				$\Delta P = -50$	$\Delta P = -100$	$\Delta P = 200$	$\Delta P = 300$
2	0.34 K	4	750	0.02	0.01	0.31	0.11
3	0.66 K	26	775	0.06	0.03	0.13	0.02

BT = brightness temperature.

between the surface and the top of the atmosphere in our algorithm. Given an atmospheric level l , we first define a channel subset (array of channel indexes \mathcal{I}_l) to use for the tests. Specifically, we retain only those selected channels for which the layer-to-space transmittances τ_l^i are within prespecified bounds, i.e. $\forall i \in \mathcal{I}_l : 0.1 < \tau_l^i < 0.4$.

In order to quantify the variability over the selected channels, we form the ensembles $\mathcal{E}_{l,1}$ and $\mathcal{E}_{l,2}$:

$$\mathcal{E}_{l,1} = \left\{ \frac{R_1^i - R_2^i}{\sigma^i} \right\}_{i \in \mathcal{I}_l} \quad \mathcal{E}_{l,2} = \left\{ \frac{R_1^i - R_3^i}{\sigma^i} \right\}_{i \in \mathcal{I}_l}, \tag{1}$$

where R_k^i is the observed radiance for channel i in the k th pixel and σ^i is the expected radiance standard deviation for the quantity $(R_1^i - R_k^i)$ in a homogeneous scene.

The so-called ‘mean test’ determines whether the absolute value of the mean of $\mathcal{E}_{l,1}$ or $\mathcal{E}_{l,2}$ exceeds a threshold T_m . The mean for a set of clear channels has an expectation value of zero and a standard deviation equal to $1/\sqrt{n_l}$, where n_l is the number of channels in \mathcal{I}_l . The values of the threshold T_m are set equal to $z/\sqrt{n_l}$, where z is a factor that can be used to estimate the number of false cloud detections in a given level by assuming normal distributions for $\mathcal{E}_{l,k}$. We selected two values of z for experiments with both simulated and real data as shown in Table 1. We chose a conservative value ($z = 2$) that is more susceptible to false cloud detections than missed clouds, and a less conservative value ($z = 3$) that is more prone to produce occurrences of cloud contamination and fewer false detections.

If the test is successful at a given level l , then the pressure at level l is defined as the effective cloud pressure. Once a cloud is detected at a level l_{cld} , we retain as clear only those channels for which $\tau_{l_{\text{cld}}}^i < 0.01$. For the clear channels, the radiances in the 3 FOVs are averaged together to reduce the effects of random instrument noise.

We attempted to develop additional tests based on the expected variance rather than the mean of the sample. However, we found that with simulated data these tests did not work well owing to the small sample size of the channel subset for a given level. We found that the mean test alone provided reasonable results using both simulated and real AIRS data.

(d) Noise filtering

With real AIRS data, we found it necessary to check for and remove noisy (outlier) channels for each sounding. To accomplish this, we perform an eigen-decomposition of brightness temperatures for the channels used in the algorithm with a subset of one full day of AIRS data. The decomposition could alternatively be done using radiances, but we have used brightness temperatures as they are more uniform across the wavelength range used.

For each profile, we reconstruct the observed brightness temperatures using only the first 40 eigenvectors. If the radiance cannot be reconstructed to within 2σ of its observed value, it is discarded from the sample. Infrequently, an extreme outlier may cause none of the channels to be accurately reconstructed. In this case, the cloud pressure is set to 100 hPa.

3. SIMULATION STUDIES

(a) *Cloudy radiance simulator*

We developed an AIRS cloudy radiance simulator to test the algorithm. In the simulator, clouds are assumed to be black. This assumption is not vital to the algorithm. The approach should work well for non-black as well as black clouds, because the algorithm depends only on horizontal variability. The choice of black clouds was a computationally inexpensive way to generate clouds in our simulations.

It would be difficult to simulate realistic subgrid variability with a global general-circulation model (GCM). Instead, we specify as free parameters for a given cloud level the cloud pressure and cloud fraction within the pixel. Up to two cloud levels were simulated per golfball. One assumption is that the two cloud pressures are the same in all adjacent pixels.

For reference, we also simulate background errors. The simulated change in brightness temperature due to background error was computed using a background-error covariance matrix similar to that of Joiner and Rokke (2000) that includes vertically correlated errors.

Random instrument noise is added according to approximate instrument specifications (0.175 K at a reference temperature of 250 K for wave number $\nu < 738 \text{ cm}^{-1}$, and 0.1 K at 250 K otherwise). These values are somewhat underestimated in the $15 \text{ }\mu\text{m}$ band as we will see in section 4. However, since the noise values are known in the simulation, increasing the noise had little effect. We did not include channel-correlated noise in our simulations.

(b) *Clear-channel identification results with Monte Carlo experiments*

We conducted Monte Carlo experiments in order to adjust the free parameters of our algorithm. We present here the results associated with the variation of the mean-test threshold parameter z .

We selected 39 profiles representative of atmospheric conditions between 18°N and 63°N . For each profile, we generated 100 background profiles (Gaussian errors added, consistent with the background-error covariance). This information is used to calculate the channel layer-to-space transmittances τ_l^i .

Using the true profiles, we compute observed radiances that correspond to the 100 profiles, 9 FOVs, and 281 channels. Two cloud levels were generated for each of the 39×100 realizations. Each cloud level is characterized by its pressure level (uniformly distributed between 980 and 200 hPa) and its cloud fraction (uniform distribution between 0 and 1 with random overlap). The observed radiances used in the cloud detection algorithm contain for each pixel contributions from the clear atmosphere, two black clouds, and instrument noise.

Figures 4(a) and (b) show the correspondence between the generated true cloud pressure level and the retrieved cloud pressure. We can see that in both simulations there is a constant offset (on the conservative side) so that clouds are frequently assigned an altitude located above the true altitude. However, for $z = 2$ there are many more

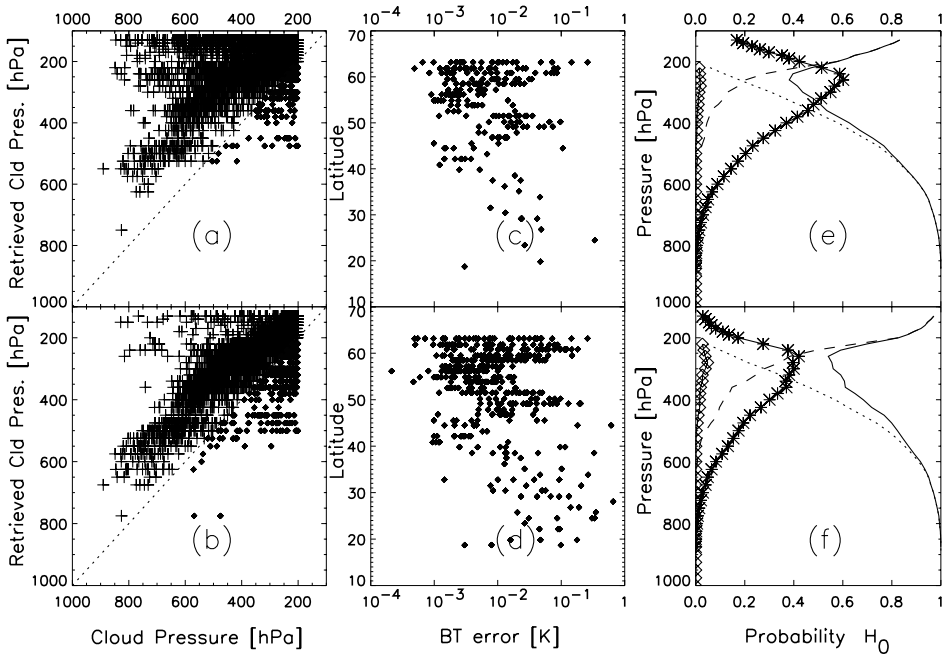


Figure 4. Results of Monte Carlo experiments. Top (bottom) row is for $z = 2$ (3). (a) and (b) Retrieved cloud pressure versus truth; plus signs (dots): clouds retrieved above (below) true altitude. (c) and (d) Brightness temperature (BT) error caused by cloud contamination in channels selected as clear. (e) and (f) Probability of correct detection (H_0 true and declared true, dots), type I error (H_0 true but declared false, diamonds), type II error (H_0 false but declared true, stars), correct non-detection (H_0 false and declared false, dashes). Solid line is the probability that the algorithm made the right decision (sum of dots and dashes). See text for details.

occurrences of clouds detected at or around 130 hPa than with $z = 3$. We can also see (as summarized in Table 1) that the algorithm never retrieves cloud pressures greater than 750 (775) hPa for $z = 2$ (3). Figures 4(a) and (b) also suggest that cases of clouds detected too low occur mostly for high clouds (300–200 hPa) and for high latitudes (see Figs. 4(c) and (d)) where the temperature profiles become more isothermal.

Figures 4(c) and (d) show, for each case, the maximum brightness temperature (BT) error caused by the presence of the clouds in the channels selected as clear. We defined the BT error as the difference between an exact observation in clear atmosphere and the observation for which cloud effect only has been added (no observation noise). We verified that when the cloud was positioned below its retrieved altitude, the BT errors were small (less than 0.03 K). The converse is that a cloud detected too low as compared to its real altitude induces larger BT errors. However, the BT errors are generally small as compared with the instrument noise. The summary in Table 1 confirms that the maximum BT error is larger for $z = 3$ than for $z = 2$, and that there are also more cases with BT errors > 0.1 K when $z = 3$.

In order to evaluate the robustness and power of our algorithm, we derived a confusion matrix for each level of the algorithm (i.e. each time the mean test is applied). For a given level l we define a hypothesis H_0 as follows: ‘There is a cloud at or above the level l ’. The robustness refers to the capacity of the algorithm to declare H_0 is true when it is true. A type I error would be declaring H_0 false when H_0 is true. The power refers to the capacity of the algorithm not to err on the side of the false detection. A type II error would be to declare H_0 true when it is false. Figures 4(e) and (f) show the four curves

corresponding to each of the four possibilities. Note that the probabilities are calculated by dividing the number of cases by the total number (3900), so that the sum of the four probabilities equals unity.

With $z = 2$ we see in Fig. 4(e) that the probability of a type II error is higher than with $z = 3$, especially for higher levels (up to 60% of the cases, instead of 40% for $z = 3$). On the other hand, the probability of a type I error is very low: less than 2% (5%), for $z = 2$ (3). Overall, the algorithm behaves better for lower levels: there are fewer cases of type II error, and the percentage of type I error remains low.

The probability of the algorithm making the right decision is impaired mainly by type II errors, rather than type I whose probability remains low. This is the intended result of a conservative algorithm design. It results in part from our conservative selection of channel transmittances ($0.1 < \tau_l^i < 0.4$) to define the sample for a given level and $0.01 < \tau_{l_{\text{cld}}}^i$ to define a cloud-contaminated channel. Therefore, the number of type II errors reported in Fig. 4 is misleading.

In order to give a better idea of how far the cloud pressure estimate is from the truth, we show in Table 1 the probability that the cloud pressure was determined within certain tolerances as compared with the true cloud pressure. For example, with $z = 3$, 13% (2%) of the time our effective cloud level is more than 200 (300) hPa above the true cloud-top level. Only 6% (3%) of the time was the retrieved effective cloud level more than 50 (100) hPa below the true cloud level.

4. RESULTS OBTAINED WITH AIRS DATA

AIRS was launched in May 2002. Shortly thereafter, the AIRS Science Team released an entire day of data (20 July 2002) known as the focus day. Results shown here are for data collected between 03 UTC and 15 UTC. We will compute $O - B$ statistics as an independent check to verify that the algorithm is performing as expected. It should be noted that $O - B$ contains errors from both observations (e.g. due to cloud contamination and instrument noise) and background information (e.g. surface temperature, emissivity, and spatial heterogeneity as well as atmospheric temperature and humidity). Although it is extremely difficult, if not impossible, to completely separate the O from the B errors, we have attempted to quantify the background errors (also including forward model errors) projected to brightness temperature space as well as the effects of instrument noise for channels with negligible contribution from the surface (see appendix A).

Observed minus background may not be sufficient to identify all cases of cloud contamination (e.g. smaller values may still contain cloud contamination as described above). For algorithms that use $O - B$ for cloud detection, values will be small (i.e. within expected ranges) by design. However, our algorithm only uses $O - B$ in cases of no contrast. Therefore, $O - B$ may be used as an independent check of the algorithm in the majority of scenes where sufficient contrast is present. In this case, large values of $O - B$, that are not necessarily excluded by our algorithm, may indicate residual cloud contamination.

For example, our algorithm may fail if a thin homogeneous cloud occurs over all nine golfball pixels above a variable cloud at a lower level. This type of problem was not present in the simulations. The simulations also showed that the algorithm will occasionally allow some cloud contamination even under ideal conditions. It is difficult to estimate how often these scenarios will occur. Observed-minus-background brightness temperature departures may provide a clue.

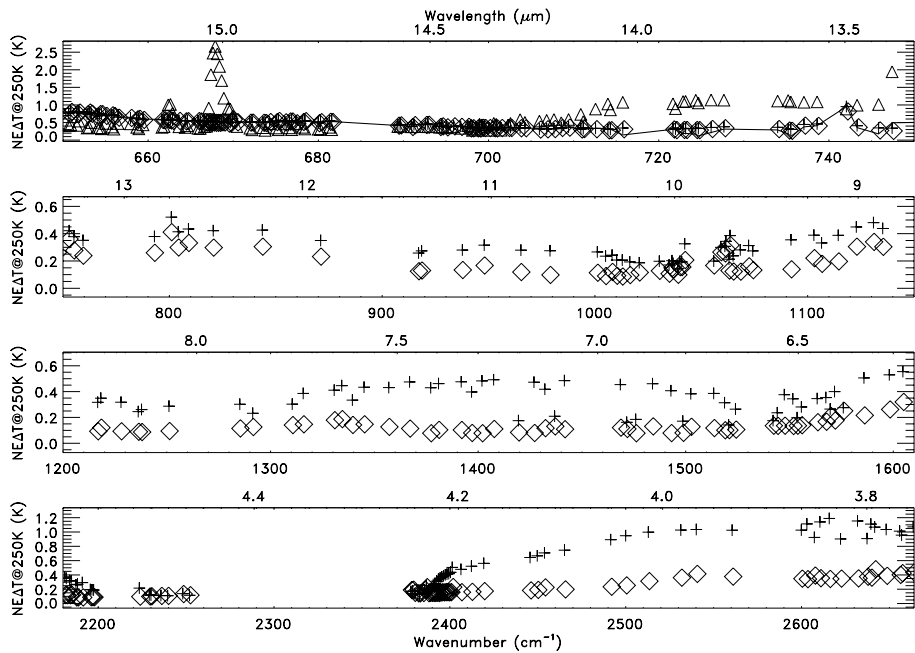


Figure 5. Estimated detector noise (diamonds) from AIRS science team and adjacent-pixel variability (+) in units of equivalent temperature at 250 K. Solid line and triangles in the top panel are estimates of detector noise and projected forecast error at 250 K (see appendix A), respectively, from observed-minus-forecast statistics.

The background B used here is a six-hour forecast from an early version of the GMAO’s finite-volume data assimilation system. The GCM includes the dynamical core of Lin (1997) with the National Center for Atmospheric Research National Center for Atmospheric Research CCM3 physics (Kiehl *et al.* 1996). The Physical-Space Statistical Analysis System (Cohn *et al.* 1998) is used to compute analysis increments. An off-line ozone analysis (Stajner *et al.* 2001) is also provided.

We use the stand-alone AIRS radiative-transfer algorithm (Strow *et al.* 2003) to compute brightness temperatures from background fields. For surface emissivity, we use values over ocean provided by Masuda *et al.* (1988). Over land, we use a database compiled from Wilber *et al.* (1999).

(a) Estimation of clear-scene adjacent-pixel variability

With real data, one must have an accurate estimate of the expected adjacent-pixel radiance differences σ_i (from Eq. (1)) in clear conditions for the cloud detection algorithm. The first step for estimating clear-sky adjacent-pixel variability is to find a subset of low-variability scenes that corresponds to either clear or overcast conditions. We define a low-variability scene as one in which selected channel brightness temperatures vary between pixels by less than a given threshold. We used one channel in the long-wave window (near 917 cm^{-1}) and one in the short-wave window (near 2657 cm^{-1}) for the variability check. The adjacent-pixel brightness temperature difference threshold was set at 0.5 K for both channels. This is an arbitrary value and, as we will see, it affects the estimated variability of surface-affected channels. Setting the threshold higher (lower) results in a larger (smaller) sample size.

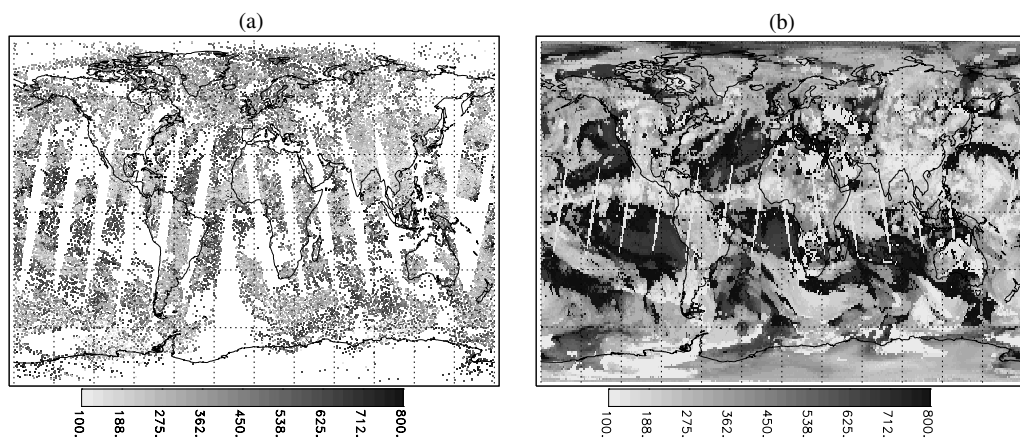


Figure 6. (a) Retrieved effective cloud pressure (hPa) from AIRS 20 July 2002. (b) Minimum cloud pressure from Aqua MODIS.

Using the selected scenes (numbering approximately 7500), we estimate the mean and r.m.s. adjacent-pixel radiance differences for each channel. The r.m.s. radiance differences are then converted to a noise-equivalent brightness temperature ($NE\Delta T$) at a reference temperature of 250 K. The values for each channel (divided by $\sqrt{2}$ to give the single FOV standard deviation) are shown in Fig. 5 along with independently derived $NE\Delta T$ s indicative of detector noise provided by the AIRS Science Team (S.-Y. Lee 2003, personal communication). We also verified that the adjacent-pixel radiance probability density functions (PDFs) were extremely Gaussian. As expected, the PDFs also had a zero mean and did not vary significantly with SZA.

The adjacent-pixel variability estimates agree remarkably with the detector noise estimates for channels in the CO_2 bands ($15\ \mu m$) that are not surface-affected. Detector noise estimates are lower than our adjacent-pixel estimates for surface-affected channels, especially those that are more moisture sensitive. This is apparently due to spatial inhomogeneity in the surface skin temperature and lower-level humidity. Smaller differences are obtained in the higher-peaking water-vapour channels due to less spatial heterogeneity. Nonlinearity of the Planck function causes larger differences between the two estimates (in terms of $NE\Delta T$ at 250 K) in the short-wave window channels.

The magnitude of the difference between the two estimates can be reduced by decreasing the value of the window channel threshold check. However, note that for the cloud detection algorithm, the surface- and humidity-sensitive channels are not used. Therefore, while it is interesting to investigate the effects of spatial inhomogeneity using the two $NE\Delta T$ estimates, it is of no consequence to the results of our study.

We note that there is one channel with anomalously high noise ($742.05\ cm^{-1}$). This channel was eliminated from the algorithm.

(b) *Derived cloud pressure and clear-channel frequency*

Figure 6 shows the retrieved effective cloud pressure derived with our algorithm. Note that this is meant to be a conservative estimate of the true cloud-top pressure. The highest clouds are seen in tropical regions just north of the equator off the west coast of Africa, over south Asia, and the Pacific.

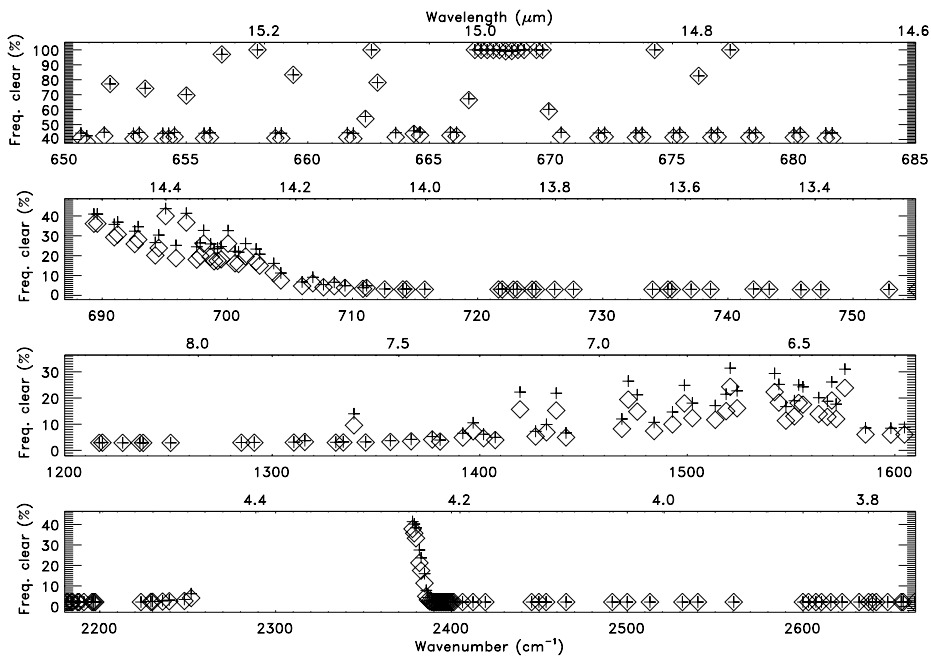


Figure 7. Frequency (%) that a channel is declared clear: diamond (+) for $z = 2$ (3).

The cloud features are very consistent with minimum cloud-top pressures derived using a CO₂ slicing technique (Menzel and Strabala 1997) from the MODIS instrument also flying on EOS-Aqua as shown in Fig. 6. The MODIS minimum cloud pressure and other MODIS cloud properties shown later are composites of 1° × 1° gridded level 3 Aqua MODIS data. The infrared MODIS pixel size is 1 × 1 km². From 60°S–60°N, either day or night orbits corresponding to the AIRS orbits shown here are used. At latitudes greater than 60°, the daily mean product is used.

The largest differences between the AIRS and MODIS cloud pressures occur in MODIS grid boxes near large gradients in cloud pressure where MODIS data indicate large subgrid variability. Because the MODIS data were averaged over a different spatial scale than the AIRS data, we were unable to make a good direct comparison between the two sets of cloud pressures.

One difference between our estimated effective cloud pressure and the minimum cloud pressure derived from MODIS is that we find fewer high cloud pressures. Our algorithm usually finds cloud pressures of less than 700 hPa, and this is consistent with the results of our simulations.

With real data, one reason for this result may be channel-correlated noise that is not accounted for in our algorithm. This correlation is significant within each read-out integrated circuit (ROIC) module, but not between modules (M. Weiler 2003, personal communication). For a given pressure, several of the channels used for the threshold tests are likely to fall within the same ROIC module. For the higher levels (lower pressures) more channels are available and therefore it is more likely to have channels spread across several different ROICs. However, at lower levels, there are fewer channels available and a higher likelihood for correlated errors to erroneously produce a cloud detection. However, this explanation does not hold for the simulations.

Figure 7 shows the frequency in percent that each channel is declared clear for the two cases $z = 2$ and 3. As in the simulations, $z = 3$ produces significantly more clear channels for channels with weighting-function peaks above the surface in the troposphere. The only channels found clear 100% of the time are those in the middle of the $15\ \mu\text{m}$ band because they always peak above the clouds. Channels peaking near the tropopause are found to be clear about 40% of the time. Upper-tropospheric humidity channels in the $6.7\ \mu\text{m}$ H_2O band are defined as clear about 10–30% of the time. In contrast, McNally and Watts (2003) find channels in this range clear up to 50% of the time. However, it should be noted that their approach requires only the centre of the nine AIRS golfball pixels to be clear, whereas our approach will declare a channel cloudy if any of the three column pixels is cloudy. Therefore, our approach may have a higher probability of being faced with cloud contamination based solely on the larger area of consideration.

The percentage of clear channels in and near window regions is about 4%. These are channels critical for determining the near-surface temperature and humidity that is important for NWP. Generally, our algorithm will find all channels with $\tau_s > 0.01$ cloudy unless a scene is declared clear. We find for a range of conditions, $\tau_s > 0.05$ for channels between 9 and $12.75\ \mu\text{m}$ and $\tau_s > 0.5$ for wavelengths $< 4.15\ \mu\text{m}$. Therefore, if a cloud is present, it will contaminate all of these channels. In these bands, we find all of these channels to be clear only about 4% of the time. The McNally and Watts (2003) algorithm finds the frequency of clear channels within these bands to vary with wavelength, e.g. channels in the $9.7\ \mu\text{m}$ band (that see the surface) clear up to 15% of the time, and some channels on the short side of $3.9\ \mu\text{m}$ clear generally less than 5% of the time. This may be a consequence of using $O - B$ to determine whether a channel is clear or cloudy.

(c) $O - B$ statistics

In order to obtain good results, we found that it was necessary to apply systematic-error correction (tuning) to correct for biases in the observations and/or forward model. We estimated tuning coefficients for each channel along the lines of Joiner and Rokke (2000). Here, we used the background over ocean downwind of areas heavily covered by radiosondes in pixels identified as clear to estimate the coefficients. The predictors for the bias correction scheme include a subset of the following for each channel: (i) constant, (ii) $\sec(\text{SZA})$, (iii) SZA, (iv) and (v) scaling factor for the optical depth of fixed gases and water vapour, respectively, used in the radiative-transfer code.

Figure 8 shows the means and standard deviations of $O - B$ for the two experiments $z = 2$ and 3. The means for the temperature sounding channels in CO_2 absorption bands are very close to zero. The standard deviations for the temperature sounding channels and window channels are very consistent at $\sim 0.7\ \text{K}$. Overall results were very similar for the two experiments. However, as will be shown later, there are more possible cloud-contaminated channels for the $z = 3$ case.

The only channels with significant biases are those in the $9.7\ \mu\text{m}$ ozone band, the $6.7\ \mu\text{m}$ water-vapour band, and temperature sounding channels that have weighting-function tails in the mesosphere. These biases are likely to be due to errors in the background field. The GMAO model is known to have a moist bias in upper levels, particularly in the Tropics, which is consistent with the positive $O - B$ bias. The positive bias in $O - B$ is inconsistent with cloud contamination, because clouds in general reduce O and thus produce negative biases. The model also has a known temperature bias at high southern latitudes in the mesosphere. This produces the negative biases in channels near the $15\ \mu\text{m}$ and $4.3\ \mu\text{m}$ band centres.

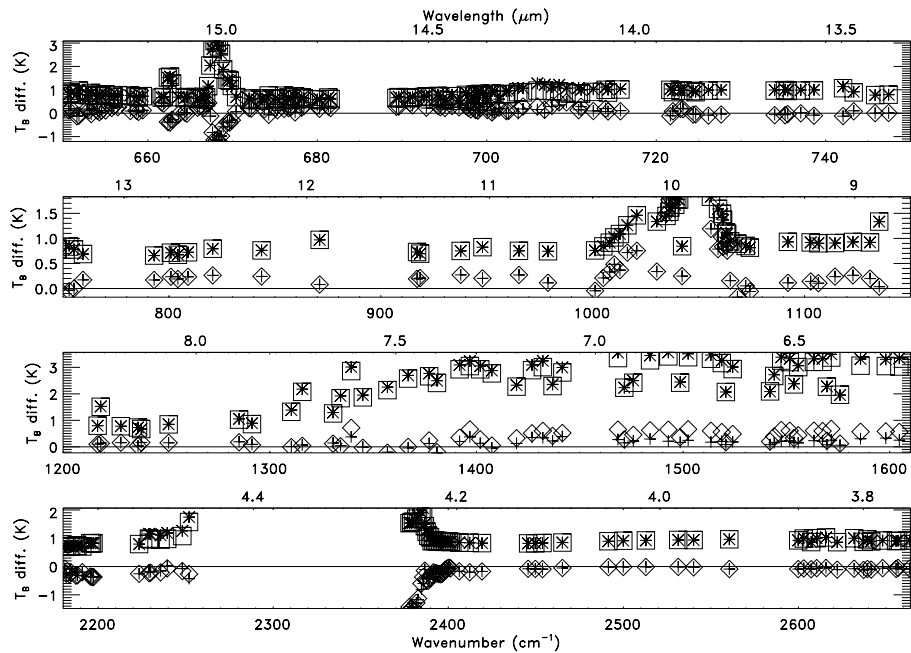


Figure 8. Observed-minus-background brightness temperature (T_B diff.) statistics. Diamond (+): mean for $z = 2$ (3); square (*): standard deviation for $z = 2$ (3).

There are slightly higher standard deviations for the $z = 3$ case for channels near 705 cm^{-1} and in the water-vapour band. For some of these channels, the bias is lower, but closer to zero for $z = 3$. This could be indicative of some cloud contamination in these channels.

Using a GMAO analysis rather than the forecast as the background gave slight improvements in $O - B$. We also computed $O - B$ for 00–03 UTC using a National Centers for Environmental Prediction analysis as the background. The mean ($O - B$)s using the two analyses as backgrounds were very similar to those shown in Fig. 8 computed with forecast background. The standard deviations were also very similar though slightly reduced when using the analyses in some of the high-peaking temperature and water-vapour channels, suggesting that the analyses are closer to the AIRS observations than the GMAO forecast. Visual inspection of maps for some channels showed isolated areas where the ($O - B$)s computed with the analyses were smaller than those using the GMAO forecast background. This demonstrates that there is information content in the AIRS data that is consistent with that from other data used in the analyses.

Figure 9 shows $O - B$ for a relatively high-peaking CO_2 channel at $14.5\text{ }\mu\text{m}$ for the $z = 2$ case. Very high tropical convective clouds contaminate this channel and most are eliminated by the algorithm. Of the 81 000 soundings, 16 (23), or roughly 0.02 (0.03)%, presented $O - B < -3\text{ K}$ for $z = 2$ (3) when the channel was identified as clear, indicating possible cloud contamination. Most of these occurred at high southern latitudes where the larger values may be due to background error. In comparison, there were 20 (25) profiles with $O - B > 3\text{ K}$, mostly at middle to high southern latitudes. There were 268 (318) sounding with $O - B > 2\text{ K}$, most at middle to high southern latitudes in an area where there appears to be background error. In contrast there were 54 (86), or 0.07 (0.1)%, with $O - B < -2\text{ K}$ for the two experiments, but these were more randomly distributed.

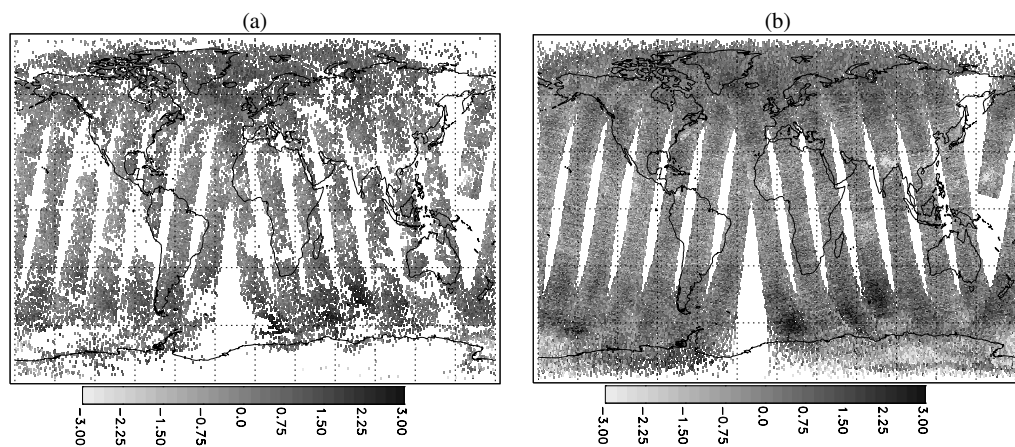


Figure 9. Observed-minus-background brightness temperatures (K) for a channel at 689.6 cm^{-1} . (a) Scenes with no contrast (clear or overcast) appear as missing data along with areas where the algorithm determines the channel to be cloud-contaminated. (b) All pixels. Values falling outside the given ranges are plotted using the minimum/maximum depth of shading.

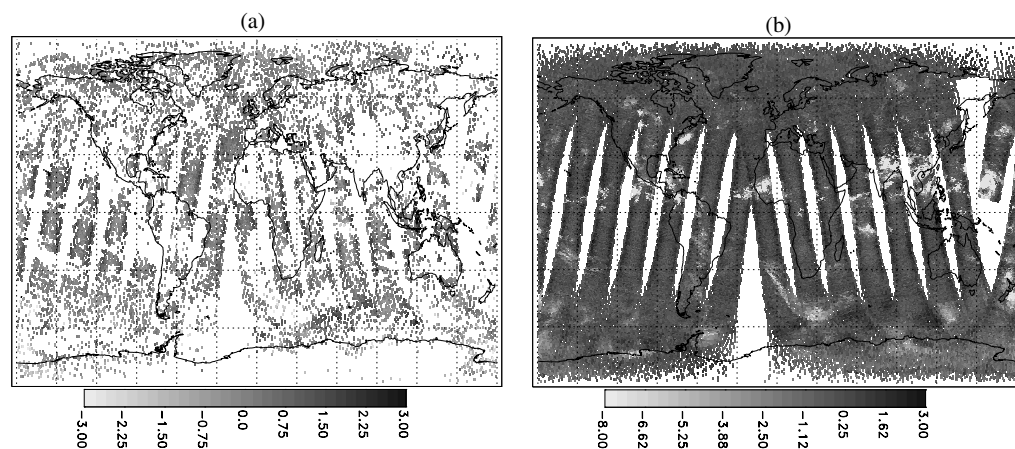


Figure 10. Similar to Fig. 9 but for a lower-peaking channel (700.6 cm^{-1}).

An indeterminate area for our algorithm (either clear or overcast as indicated by an insufficient amount of contrast in the adjacent pixels) occurs near 70°S , 140°W . This and other similar areas show as missing data in Figs. 9–11. In a case such as this, if the scene does not pass the strict clear checks described above, our algorithm defaults to a conservative cloud pressure of 100 hPa.

Figure 10 shows $O - B$ for a channel centred at 700.6 cm^{-1} , peaking lower in the atmosphere. There is significantly more cloud contamination in this channel, but also a significant number of soundings determined to be clear. For this channel, there were 49 (154) soundings with $O - B < -3\text{ K}$ for $z = 2$ (3) when it was determined to be clear, most at high latitudes. There were 0 (0) soundings with $O - B > 3\text{ K}$. There were 184 (422) soundings with $O - B < -2\text{ K}$, most at high southern latitudes and 61 (66) soundings with $O - B > 2\text{ K}$, most at low latitudes. This suggests that there are very few possible cases of cloud contamination for the $z = 2$ case, but potentially

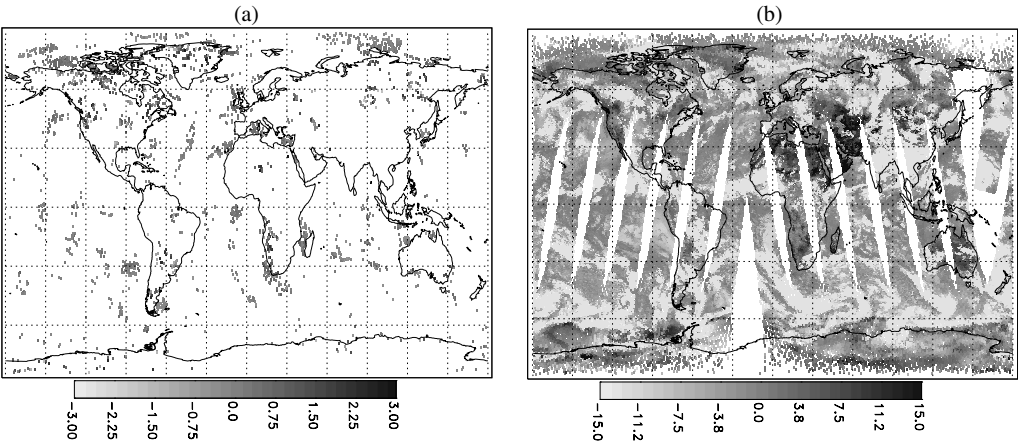


Figure 11. Similar to Fig. 9 but for an 11 μm window channel (917.1 cm^{-1}).

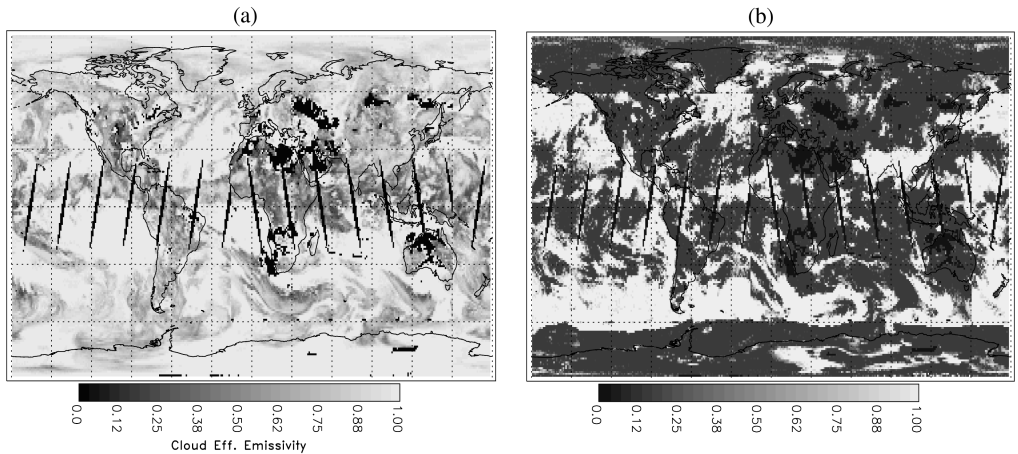


Figure 12. (a) Mean effective emissivity derived from Aqua MODIS. (b) minimum cloud fraction from MODIS.

more when $z = 3$. Visually, one can see that this channel is declared clear in regions that appear to be cloudy. It is not clear whether the channel is contaminated due to possible homogeneous high thin cloud over an inhomogeneous lower cloud or whether the model has a warm bias over these cloudy regions.

Figure 11 shows $O - B$ for an 11 μm window channel. For this channel to be identified as clear, it must pass all clear tests in addition to the homogeneity test. By definition of the background checks, this channel must be within 1 K of the background over ocean and within 3 K over land. Many of the areas over land identified as clear by MODIS pixels are not found to be clear with AIRS. These pixels fail to pass the background check due to significant errors in the background skin temperatures. Note that MODIS finds very few $1^\circ \times 1^\circ$ grid points to be completely cloud free. Most of the areas identified as clear in our algorithm correspond to areas where the MODIS minimum cloud fraction, shown in Fig. 12, is very low or zero.

One area where our results differ from those of McNally and Watts (2003) is along the middle orbit that overpasses Africa. They find the $13.5\text{ }\mu\text{m}$ channel to be frequently clear over central and northern Africa, whereas we find this channel to be mostly cloudy. This channel should be clear only if there are low or no clouds present. Figure 6 shows that there are few low clouds in the MODIS minimum cloud-pressure product in this area. Our algorithm similarly finds high clouds along the orbit. Low values of effective emissivity (product of the emissivity and cloud fraction) are derived from MODIS, as shown in Fig. 12, in the region indicating broken or thin cloud that may be difficult to detect with an $O - B$ approach.

There are some areas identified as clear by our algorithm and also by that of McNally and Watts (2003) that are not identified as clear in MODIS products. One example is the area near 50°S , 100°W . The MODIS minimum cloud fraction in the area was not always low, the mean emissivity was relatively high, and the minimum cloud pressures were between 850 and 900 hPa. In such night-time cases, it is difficult to determine whether cloud was indeed present.

5. SUMMARY AND FUTURE WORK

We have developed a new clear-channel identification scheme and applied it to both real and simulated AIRS data. The algorithm is relatively easy to implement, does not require substantial computational resources, and is mostly background-independent. It searches for spatial variability induced by the presence of clouds. It can be applied alone or in conjunction with ($O - B$)-based cloud detection schemes. The threshold parameters can be adjusted to more or less conservative values based on the particular application.

Because the approach uses information from adjacent pixels, the full pixel complement within an AIRS/AMSU golfball is desired. For our implementation, at least three of the nine pixels are required. It is desirable to retain as many channels as possible in the CO_2 bands from the original dataset. The results obtained here may be improved with a larger subset of channels. Our simulations showed small improvements when the full AIRS channel complement in the selected CO_2 bands is used.

The $O - B$ brightness temperature statistics have been used as an independent check and suggest that the algorithm is performing well. In addition, the derived conservative cloud pressure estimate compared well with retrieved minimum cloud pressures from Aqua MODIS.

The ultimate test of any cloud detection method for NWP and climate application is to evaluate the impact within a data assimilation system. We have implemented the new clear-channel identification within a one-dimensional variational cloud-clearing analysis and assimilation scheme. We plan to conduct impact assessments in the near future.

The method developed here may have applications for other types of instruments. For example, it is important to have an accurate cloud mask for ultraviolet instruments that are used to derive information about trace gases and aerosol. We plan to explore adjacent-pixel homogeneity tests for cloud masking using the ultraviolet Ozone Monitoring Instrument that will fly on EOS Aura.

ACKNOWLEDGEMENTS

The authors thank the AIRS science team, especially M. Goldberg and W. Wolf, for providing the AIRS radiance data soon after launch. We also thank Goddard Distributed Active Archive Center and A. Gopalan for promptly providing Aqua MODIS data and

associated software. Finally, the comments of two anonymous reviewers are appreciated as they have helped to improve the manuscript. This work was supported by a grant from NASA.

APPENDIX

Estimating forecast error in AIRS channels

Using $O - B$ statistics from two different experiments, we can derive the projected forecast error onto AIRS channels in the $15\ \mu\text{m}$ band. Within this band, clear-scene adjacent-pixel variability is due mainly to detector noise as illustrated in Figs. 5.

In addition to computing $O - B$ for clear channels using O as an average of the radiances in the three column pixels, we also computed $O - B$ with O as the radiance from the clearest pixel. The $O - B$ variance for a particular channel for the latter experiment with the single pixel observation (σ_1^2) may be expressed by

$$\sigma_f^2 + \sigma_o^2 = \sigma_1^2, \quad (\text{A.1})$$

and for the former experiment where three pixels are averaged (σ_3^2) by

$$\sigma_f^2 + \sigma_o^2/3 = \sigma_3^2, \quad (\text{A.2})$$

where σ_f^2 is the variance of the projected forecast error and σ_o^2 is the detector noise. These equations assume that forecast and observation errors are uncorrelated and that the forecast errors are constant. Since forecast errors are known to vary spatially, the estimates obtained here can be considered as a global average. The solutions to these equations are

$$\sigma_o = \sqrt{1.5\sigma_1^2 - 1.5\sigma_3^2} \quad (\text{A.3})$$

and

$$\sigma_f = \sqrt{1.5\sigma_3^2 - 0.5\sigma_1^2}. \quad (\text{A.4})$$

We solve all equations using radiances rather than brightness temperatures, because detector noise should be constant in radiance units. The values of σ_o and σ_f are then converted to an equivalent temperature value at 250 K to be consistent with other error estimates.

The top panel of Fig. 5 ($15\ \mu\text{m}$ band) shows the estimates of σ_o (solid line) and σ_f (triangles) from this approach. The values of σ_o are extremely consistent with the estimates of detector noise from the AIRS science team and adjacent-pixel variability. This gives us confidence in our estimate of σ_f .

The channels peaking in the upper troposphere and lower stratosphere (around 660 and $680\ \text{cm}^{-1}$) have detector noise estimates slightly higher than projected forecast errors. Channels peaking in the upper stratosphere (near the $15\ \mu\text{m}$ band centre) and lower troposphere (on the short side of about $14.3\ \mu\text{m}$), in contrast, have significantly lower estimates of detector noise than the forecast errors.

Note that the values of σ_f shown here cannot be compared directly with the estimates of McNally and Watts (2003) who used an estimate of the European Centre for Medium-Range Weather Forecasts background error projected to AIRS brightness temperatures. The latter estimates are valid at temperatures corresponding to representative observations rather than 250 K. However, for channels with observed brightness temperatures near 250 K (peaking in the middle troposphere near $710\ \text{cm}^{-1}$), the two may be compared. Our estimated σ_f values are comparable or slightly higher for these channels.

REFERENCES

- Aumann, H. H. and Pagano, R. J. 1994 Atmospheric Infrared Sounder on the Earth Observing System. *Opt. Eng.*, **33**, 776–784
- Chahine, M. T. 1974 Remote sounding cloudy atmospheres. I: The single cloud layer. *J. Atmos. Sci.*, **31**, 233–243
- 1977 Remote sounding cloudy atmospheres. II: Multiple cloud formations. *J. Atmos. Sci.*, **34**, 744–757
- Chevallier, F., Bauer, P., Mahfouf, J. F. and Morcrette, J. J. 2002 Variational retrieval of cloud profile from ATOVS observations. *Q. J. R. Meteorol. Soc.*, **128**, 2511–2525
- Cohn, S. E., da Silva, A. M., Guo, J., Sienkiewicz, M. and Lamich, D. 1998 Assessing the effects of data selection with the DAO Physical-space Statistical Analysis System. *Mon. Weather Rev.*, **126**, 2913–2926
- Derber, J. and Wu, W.-S. 1998 The use of cloud-cleared radiances in the NCEP SSI analysis system. *Mon. Weather Rev.*, **126**, 2287–2299
- English, S. J., Eyre, J. R. and Smith, J. A. 1999 A cloud-detection scheme for use with satellite sounding radiances in the context of data assimilation for numerical weather prediction. *Q. J. R. Meteorol. Soc.*, **125**, 2359–2378
- Goldberg, M. D., Qu, Y., McMillin, L. M., Wolf, W., Zhou, L. and Divakarla, M. 2003 AIRS Near-real-time products and algorithms in support of operational numerical weather prediction. *IEEE Trans. Geosci. Rem. Sens.*, **41**, 379–389
- Joiner, J. and da Silva, A. M. 1998 Efficient methods to assimilate remotely sensed data based on information content. *Q. J. R. Meteorol. Soc.*, **125**, 1669–1694
- Joiner, J. and Rokke, L. 2000 Variational cloud clearing with TOVS data. *Q. J. R. Meteorol. Soc.*, **126**, 725–748
- Kiehl, J. T., Hack, J. J., Bonan, G. B., Boville, B. A., Briegleb, B. P., Williamson, D. L. and Rasch, P. J. 1996 Description of the NCAR Community Climate Model (CCM3). NCAR Technical Note, NCAR/TN-420+STR, Boulder, CO
- Lin, S.-J. 1997 A finite-volume integration method for computing pressure gradient forces in general vertical coordinates. *Q. J. R. Meteorol. Soc.*, **123**, 1749–1762
- McMillin, L. M. and Dean, C. 1982 Evaluation of a new operational technique for producing clear radiances. *J. Appl. Meteorol.*, **21**, 1005–1014
- McNally, A. P. and Watts, P. D. 2003 A cloud detection algorithm for high-spectral-resolution infrared sounders. *Q. J. R. Meteorol. Soc.*, **129**, 3411–3423
- Masiello, G., Serio, C. and Shimoda, H. 2003 Qualifying OMG tropical spectra for clear sky. *J. Quant. Spectrosc. Rad. Trans.*, **77**, 131–148
- Masuda, K., Takashima, T. and Takayama, Y. 1988 Emissivity of pure and sea waters for the model sea surface in the infrared window regions. *Remote Sens. Environ.*, **24**, 313–329
- Menzel, P. and Strabala, K. 1997 Cloud top properties and cloud phase algorithm theoretical basis document. NASA MODIS document ATBD-MOD-04, Greenbelt, MD, USA. <http://modis-atmos.gsfc.nasa.gov>
- Menzel, P., Wylie, D. P. and Strabala, K. I. 1992 Seasonal and diurnal changes in cirrus clouds as seen in four years of observations with the VAS. *J. Appl. Meteorol.*, **31**, 370–385
- Prunet, P., Thépaut, J.-N. and Cassé, V. 1998 The information content of clear sky IASI radiances and their potential for numerical weather prediction. *Q. J. R. Meteorol. Soc.*, **124**, 211–241
- Smith, W. L. 1968 An improved method for calculating tropospheric temperature and moisture from satellite radiometer measurements. *Mon. Weather Rev.*, **96**, 387–396
- Stajner, I., Riishøjgaard, L. P. and Rood, R. B. 2001 The GEOS ozone data assimilation system: Specification of error statistics. *Q. J. R. Meteorol. Soc.*, **127**, 1069–1094
- Stow, L. L., Hannon, S. E., De Souza-Machado, S., Motteler, H. E. and Tobin, D. 2003 An overview of the AIRS radiative transfer model. *IEEE Trans. Geosci. Rem. Sens.*, **41**, 303–313
- Wilber, A. C., Kratz, D. P. and Gupta, S. K. 1999 Surface emissivity maps for use in satellite retrievals of longwave radiation. NASA Tech. Pub. 1999-209362, Hanover, MD, USA. <http://www.sti.nasa.gov>